Research Square

Preprints are preliminary reports that have not undergone peer review.
They should not be considered conclusive, used to inform clinical practice,
or referenced by the media as validated information.

Development of OpenMC based AI Model for Gamma Spectral Decomposition for Low Activity Estimation in Environmental Samples

Danish Gulzar
Pakistan Institute of Engineering and Applied Sciences
Muhammad Sohail
msohailafzal@gmail.com
Pakistan Institute of Engineering and Applied Sciences
Awais Zahur
Pakistan Institute of Engineering and Applied Sciences
Rizwan Ahmed
Pakistan Institute of Engineering and Applied Sciences

Research Article

Keywords: Radioisotope identification, Activity estimation, NaI(Tl) scintillation detector, Deep learning ensemble, OpenMC

Posted Date: November 18th, 2026

DOI: https://doi.org/10.21203/rs.3.rs-11647722/v1

License: This work is licensed under a Creative Commons Attribution 4.0 International License.
Read Full License

Additional Declarations: No competing interests reported.

Development of OpenMC based AI Model for Gamma Spectral Decomposition for Low Activity Estimation in Environmental Samples

Danish Gulzar, Muhammad Sohail*, Awais Zahur, Rizwan Ahmed

[a]*Department of Nuclear Engineering, Pakistan Institute of Engineering & Applied Sciences (PIEAS), Nilore, Islamabad 45650, Pakistan*

* Corresponding author

e-mail: msohailafzal@gmail.com

Tel:+92-51-9593745

Cell: +92-344-5280342

Fax: +92-51-9248600

Names

1. Danish Gulzar

Email: danishgulzarpieas@gmail.com

Department of Nuclear Engineering, Pakistan Institute of Engineering & Applied Sciences (PIEAS), Nilore, City: Islamabad 45650, Country: Pakistan

2. Muhammad Sohail

Email: msohailafzal@gmail.com

Department of Nuclear Engineering, Pakistan Institute of Engineering & Applied Sciences (PIEAS), Nilore, City: Islamabad 45650, Country: Pakistan

3. Awais Zahur

Email: awais@pieas.edu.pk

Department of Nuclear Engineering, Pakistan Institute of Engineering & Applied Sciences (PIEAS), Nilore, City: Islamabad 45650, Country: Pakistan

4. Rizwan Ahmed

Email: rizwanahmed@pieas.edu.pk

Department of Nuclear Engineering, Pakistan Institute of Engineering & Applied Sciences (PIEAS), Nilore, City: Islamabad 45650, Country: Pakistan

Keywords:

Radioisotope identification, Activity estimation, NaI(Tl) scintillation detector, Deep learning ensemble, OpenMC

Abstract

Bulk gamma-ray spectrometry of environmental soil samples using sodium iodide detectors is limited by severe photopeak overlap, density-dependent self-absorption and the lack of certified volumetric calibration standards for trace fallout. In this study, a computational framework couples OpenMC particle transport modeling of a cylindrical NaI(Tl) crystal in sealed polymer Marinelli container geometry with an AI-based spectrum decomposition (AI-SD) architecture. Twenty-three environmental soil samples characterized by high-purity germanium (HPGe) spectrometry served as an experimental reference for validating simulated response functions of principal radionuclides (^{226}Ra, ^{232}Th, ^{40}K and ^{137}Cs). A dataset of 100,000 synthetic spectra spanning variable bulk soil densities was generated to train a heterogeneous soft-voting ensemble combining 1D-CNN peak-shaping filters, residual baseline-preservation pathways and an attention-gated U-Net deconvolution network. Dynamic attention gating selectively isolates the 661.7 keV ^{137}Cs photopeak from adjacent 609.3 keV ^{214}Bi down-scattering without requiring empirical background subtraction. Across an independent synthetic test set of 15,000 spectra, the ensemble achieved 100% identification accuracy with mean absolute percentage errors below 4.3% for primordial decay series and 96.5% accuracy (0.81 Bq/kg mean absolute error) for trace ^{137}Cs. When benchmarked against 21 intact physical soil samples, the framework demonstrated strong agreement with laboratory HPGe measurements ($R^2 > 0.98$), completely eliminating the uranium-series divergence typical of classical matrix unfolding. Executing in under 10 ms per spectrum on standard central processing units, the methodology provides a practical calibration equivalent for autonomous environmental soil radiometry.

1. Introduction

Radiological surveillance of environmental soil is essential for evaluating environmental safety, assessing population dose rates and identifying anthropogenic contamination (Shabbir et al., 2023; UNSCEAR, 2000). Assessing bulk soil radioactivity demands analytical techniques capable of resolving multi-emitter decay cascades (^{238}U and ^{232}Th series) alongside naturally abundant ^{40}K and trace fission products such as ^{137}Cs (Knoll, 2010).

Laboratory characterization of soil samples traditionally relies on high-purity germanium (HPGe) semiconductor detectors due to their high energy resolution (Shabbir et al., 2023). However, the need for liquid nitrogen cooling, high equipment costs and operational complexity limits their use in high-throughput screening and autonomous field deployment. In contrast, thallium-doped sodium iodide scintillators operate reliably at ambient temperatures, provide higher geometric counting efficiency and offer cost-effective instrumentation (Knoll, 2010). The main limitation of NaI(Tl) scintillators in bulk soil measurements is their moderate energy resolution, which causes severe photopeak broadening and masks low-yield emissions beneath the Compton scattering continuum.

To recover incident gamma-ray distributions from broadened scintillation pulse-height spectra, spectrum unfolding techniques solve the ill-posed inverse problem relating recorded detector responses to incident source activities. Established classical unfolding methodologies include discrete response matrix inversion, sequential spectral stripping, iterative regularized algorithms (such as Gold's deconvolution and maximum entropy unfolding) and full-spectrum least-squares fitting. In environmental radiation monitoring, researchers have applied these numerical unfolding approaches to interpret composite NaI(Tl) spectra acquired from bulk geological and soil media (Muminov et al., 2005; Naeem et al., 2025).

Among these approaches, Full-Spectrum Analysis (FSA) models the composite pulse-height distribution as a linear superposition of pre-measured standard library spectra using weighted non-negative least-squares optimization across broad energy intervals (Allyson & Sanderson, 1998; Caciolli et al., 2012; Cresswell et al., 2006; Guastaldi et al., 2013; Hendriks et al., 2001; Kock & Samuelsson, 2011; Minty, 1992). By incorporating all recorded counts rather than isolated photopeak windows, FSA substantially improves statistical precision and reduces counting uncertainty for low-activity measurements. However, because library shapes are experimentally calibrated for fixed physical matrices, uncompensated variations in soil bulk density, moisture content or elemental composition alter self-attenuation, causing spectral

mismatch that introduces severe systematic quantification bias (Cresswell et al., 2006; Minty, 1992).

Conversely, spectral stripping matrices and numerical spectrum decomposition deconvolute overlapping components through direct algebraic matrix transformations or sequential high-to-low energy subtraction (IAEA, 2003; Muminov et al., 2005; Naeem et al., 2025). While computationally straightforward and capable of rapidly isolating dominant photopeaks without non-linear fitting, these linear techniques exhibit severe numerical instability in environmental media. In sequential stripping, Poisson counting errors propagate cumulatively downward into low-energy channels, while ill-conditioned response matrices cause matrix inversion to diverge, producing large analytical variance and erratic activity estimates across natural decay series (Naeem et al., 2025).

Crucially, both full-spectrum fitting and matrix deconvolution share a fundamental bottleneck: their strict requirement for certified physical calibration standards prepared in identical container geometries and matching sample bulk densities (Naeem et al., 2025). Such volumetric reference materials are rarely available for trace anthropogenic fallout (^{137}Cs) dispersed within natural soil matrices, leaving trace fission products omitted or uncalibrated in classical scintillation assays.

Machine learning and deep neural networks provide a practical approach to overcome physical calibration constraints in gamma-ray spectrometry. Networks trained on computationally modeled detector responses learn direct relationships relating pulse-height distributions directly to isotopic activities (Kamuda et al., 2020). Over the past decade, one-dimensional network configurations primarily convolutional filters, residual layers and multi-scale contraction-expansion models have shown promising capabilities in automated spectral feature extraction.

One-dimensional Convolutional Neural Networks (1D-CNNs) extract spectral features by applying convolutional filters across consecutive energy channels (Kamuda et al., 2020). These convolutional operations automatically capture localized peak curvatures and characteristic Compton edges without relying on preset energy windows. Computational experiments confirmed that convolutional filters remain stable under fluctuating counting statistics and low-amplitude background noise. However, most previous convolutional models have been designed strictly for radionuclide classification rather than simultaneous activity quantification or spectral line deconvolution.

Similarly in order to train deeper networks while mitigating vanishing gradients, residual architectures incorporating identity shortcut connections were introduced to radiation spectroscopy (Kamuda et al., 2020). These shortcut connections allow spectral features to pass directly through network layers, helping the model to preserve the continuous baseline continuum shape of the spectrum. Published benchmarks have shown that residual layers are sensitive to low-yield gamma emissions embedded within elevated backgrounds. Still, current residual models remain confined to categorical library identification and cannot separate overlapping Compton down-scattering from discrete photopeak emissions.

For the cases of non-linear spectral deconvolution and line restoration, the contracting-expanding networks such as 1D U-Net architectures have shown reliable results (Ronneberger et al., 2015). By bridging down-sampling compression stages with symmetric up-sampling expansion layers through horizontal skip connections, U-Net retains high-frequency spatial peak coordinates (Ronneberger et al., 2015). This architecture avoids the numerical instability and noise amplification as expected by iterative matrix unfolding algorithms. However, published U-Net implementations have operated strictly as separate deconvolution algorithms, without integrating automated detection thresholding or specific activity regression.

However, our work has treated convolutional, residual and encoder-decoder topologies as separate and single-purpose algorithms. No unified computational system currently integrates these distinct architectures into a consolidated multi-objective pipeline designed for bulk soil gamma spectrometry. The classical matrix deconvolution in general encounters error amplification when isolating trace fallout from intense natural decay series without empirical reference standards (Naeem et al., 2025). Hence this investigation develops a calibration free AI-based spectrum decomposition (AI-SD) framework by combining 1D convolutional layers, residual shortcut paths and an attention-gated 1D U-Net equipped with 1D-CBAM channel and spectral attention mechanisms (Woo et al., 2018).

In this study, a transport-calibrated computational methodology is established for automated bulk soil radiometry. First, a detailed Monte Carlo model of a cylindrical sodium iodide crystal (2″ × 2″) enclosed within a sealed polymer Marinelli container geometry was constructed in OpenMC (Romano et al., 2015) across variable bulk densities (1.10–1.80 g/cm³). This model after validation was used to synthesize 100,000 composite pulse-height distributions covering global environmental NORM ranges and trace ^{137}Cs from fallout including realistic Poisson counting fluctuations. A heterogeneous soft-voting ensemble was then trained under multi-task loss optimization to simultaneously govern radionuclide presence gating, quantify mass-

normalized specific activities (Bq/kg) and deconvolve composite soil spectra into pure isotopic lines.

Section 2 describes the OpenMC soil transport modeling, polymer Marinelli container specifications, density self-absorption corrections and physical soil sample measurements. Section 3 presents the synthetic dataset generation, spectral preprocessing, deep network topologies and multi-task loss formulation. Section 4 provides the performance evaluation across baseline synthetic metrics, 23 physical environmental soil samples, comparative benchmarks against classical deconvolution and photomultiplier gain drift.

2. Computational Modeling and Measurements

A detailed Monte Carlo transport model of the scintillation detector and bulk soil sample was developed using the OpenMC radiation transport package (Romano et al., 2015). Figure 1 shows the cross-sectional geometry of the detector assembly, sealed polymer Marinelli container and graded lead shield used for the OpenMC runs. To replicate surface charge recombination effects, an uncollected frontal boundary layer was specified on the crystal, surrounded by a magnesium oxide optical diffusion reflector and an aluminum protective jacket. All physical dimensions of the computational model are summarized in Table 1.

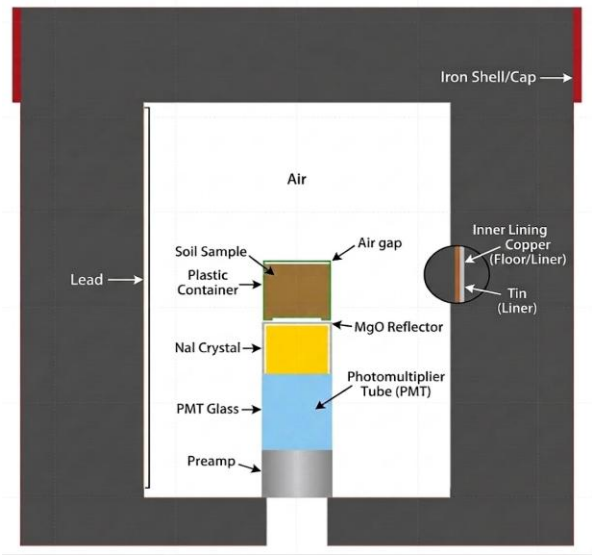


Figure 1. Cross-sectional geometry of the OpenMC detector assembly, sealed polymer Marinelli container and lead shield.

Table 1. Physical dimensions of the OpenMC computational model.

Component	Material	Dimensions and Specifications
Soil sealed container	Polymer	R = 2.8 cm, H = 6.3 cm, Wall thickness: 1.0 mm
Detector–Beaker Gap	Air	1.5 mm axial air gap
Lead Base	Lead (Pb)	18″ × 9″ × 2″
Shielding Rings (16×)	Lead (Pb)	Inner R = 12.7 cm, Outer R = 22.86 cm, Pitch: 2.5 cm
Graded Liner	Sn + Cu	0.25 mm Sn + 0.25 mm Cu
Top Shielding Lid	Lead (Pb)	4 discs (10.0 cm total thickness)
Structural Shell	Iron (Fe)	0.5 mm thickness

The bulk soil sample was modeled within a sealed polymer Marinelli container surrounding the detector crystal as shown in Table 1. The geochemical composition of the soil sample was defined using the standard continental rock specification from the PNNL Materials Compendium (McConn et al., 2011), with the oxide and elemental mass fractions summarized in Table 2.

Table 2. Oxide and elemental composition of the modeled soil sample (McConn et al., 2011).

Oxide	Oxide (wt%)	Element	Elemental (wt%)
SiO_2	70.0	*Si*	32.75
Al_2O_3	15.0	*Al*	7.94
CaO	5.0	*Ca*	3.57
Fe_2O_3	5.0	*Fe*	3.50

K_2O	3.0	*K*	2.49
MgO	2.0	*Mg*	1.21
—	—	*O*	50.50
Total	100.0%	Total	100.00%

The photon attenuation in soil is governed primarily by incoherent Compton scattering across the relevant gamma-ray energy spectrum (Knoll, 2010). Whereas the average atomic-to-mass number ratio ($Z/A \approx 0.49$) is nearly constant across natural rock-forming elements with minor geochemical variations resulting in negligible variations in mass attenuation coefficients (Hubbell & Seltzer, 1995). Therefore, the volumetric self-attenuation inside the sample container depends primarily on bulk density. In order to account for the environmental density variations the response functions were computed across the expected soil density envelope around the nominal 1.50 g/cm³ baseline. The surrounding shielding was modeled as a lead castle constructed from interlocking rings with a graded tin-copper liner as details in Table 1.

The ENDF/B-VII.1 cross-section data library was used to simulate the photon interactions within OpenMC's continuous-energy transport treatment (Chadwick et al., 2011). Bremsstrahlung photon production from secondary electrons was treated via thick-target approximations hence reducing tracking time while preserving spectral shape. Interaction events were scored in the active NaI(Tl) crystal volume using pulse-height tallies. Each tally tracked 1.0×10^7 primary photon histories to ensure the relative statistical error in the photopeaks remained below 1%.

Seven individual pulse-height tallies were computed for the primary decay daughters: ^{214}Pb and ^{214}Bi (^{238}U series), ^{212}Pb, ^{208}Tl and ^{228}Ac (^{232}Th series), ^{40}K and ^{137}Cs. These tallies were combined into parent isotope response functions using decay chain branching ratios. The ^{208}Tl contribution was scaled by its 35.94% branching ratio. In addition, a 30% ^{222}Rn diffusion loss correction was applied to the ^{238}U daughter tallies to account for the Radon gas escape through the sealed polymer containers.

The scintillator energy resolution across incident photon energies, E (keV) was parameterized according to the empirical broadening function (Dietze & Klein, 1982; Knoll, 2010), using Eq. (1):

$$FWHM(E) = a + b\sqrt{E} \quad (1)$$

where a = *-6.64* and b = *2.20* were determined from calibration measurements. An asymmetric exponential tail with an 18% fraction and a decay constant (τ = *60 keV)* was applied to account for photo-electron escape and crystal edge scattering.

To account for bulk density variations across diverse soil types, the energy-dependent mass attenuation coefficient $\mu_\rho(E)$was parameterized from standard photon cross-section data (Hubbell & Seltzer, 1995). Mass attenuation coefficients for the soil composition (Table 2) were extracted from the NIST XCOM database across the detector operating energy range. A log-linear least-squares regression of $\ln(\mu_\rho)$ against $\ln(E_{\mathrm{MeV}})$ yielded an empirical power-law parameterization ($R^2 = 0.994$), expressed in Eq. (2):

$$\mu_\rho(E) = \exp[-0.42\ln(E_{MeV}) - 2.76] \quad (2)$$

where E_{MeV}denotes incident photon energy in MeV. Volumetric response spectra were adjusted for density variations by applying an exponential self-absorption factor based on the bulk density deviation from the baseline across the effective path length through the sealed polymer Marinelli container cavity.

The computational detector response model was validated against experimental calibration spectra acquired with an ORTEC 927 multichannel analyzer (MCA) and MAESTRO software. As all physical measurements were conducted at low count rates hence the dead-time fractions under 2%, pulse pile-up was negligible which ensures the linear response of the detection system.

The physical sample set included 23 environmental soil samples collected from the Nilore region, Pakistan (Naeem et al., 2025; Shabbir et al., 2023). Baseline specific activities (Bq/kg) were established by High-Purity Germanium (HPGe) spectrometry (Shabbir et al., 2023). Each sample was counted in a sealed polymer Marinelli container for 86,400 seconds (24 hours). Twenty-one samples (with sample masses ranging between 0.159 and 0.211 kg) formed the primary quantitative evaluation set, while two samples exhibiting physical sample anomalies were evaluated separately as outliers. Figure 2 displays the acquired gamma-ray spectrum of Sample No. 9, exhibiting pronounced photopeak overlap and elevated Compton down-scattering throughout the acquisition interval. For trace ^{137}Cs, baseline activities were decay-corrected to the NaI(Tl) counting epoch over the 5.8-year interval based on the 30.17-year half-life of ^{137}Cs (Knoll, 2010), resulting in a decay correction factor of 0.8712.

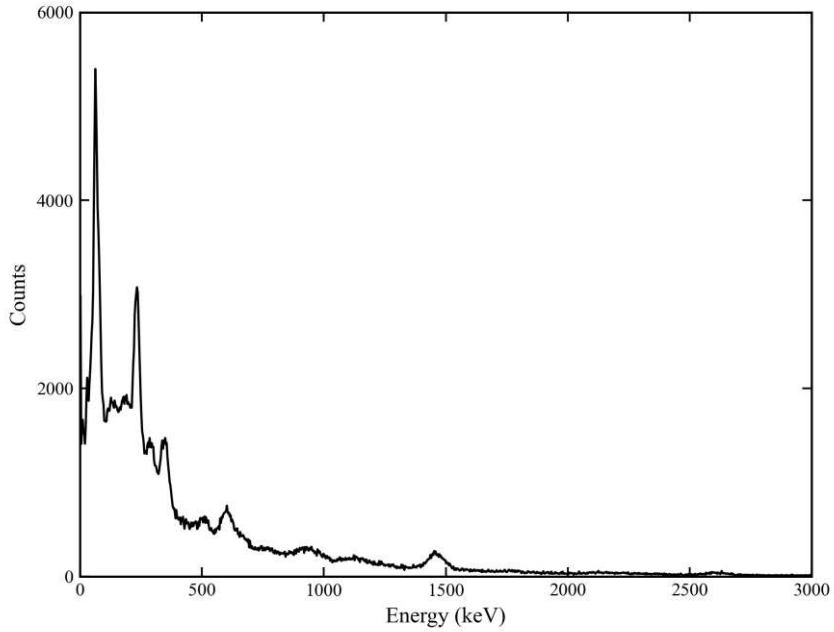


Figure 2. Measured NaI(Tl) gamma-ray spectrum of Singhot Syedan soil (sample No. 9).

3. Deep Learning Framework

The OpenMC computational model was validated and synthetic dataset was generated across the specified soil bulk density range. Specific activities for naturally occurring radionuclides were uniformly sampled across global environmental soil ranges established by UNSCEAR (2000): ^{226}Ra (10.0–150.0 Bq/kg), ^{232}Th (15.0–200.0 Bq/kg) and ^{40}K (100.0–1500.0 Bq/kg). Anthropogenic ^{137}Cs was sampled using a log-normal distribution (0.2–25.0 Bq/kg) with a 35% true absence fraction to replicate near threshold environmental fallout. Operating within this verified linear response regime justifies the use of linear superposition to calculate the composite soil spectrum $S_{comp}(E)$ (Hendriks et al., 2001; Muminov et al., 2005), as given in Eq. (3):

$$S_{comp}(E) = \sum_{i=1}^{4} A_i \cdot R_i(E) + B(E) \quad (3)$$

where A_i represents the sampled specific activity (Bq/kg) of each target radionuclides, $R_i(E)$ is the corresponding unit response function computed by OpenMC and $B(E)$ is the 24 hour measured background spectrum with added Poisson noise. This procedure generated a total dataset of 100,000 composite spectra, divided into 70% for training (70,000 spectra), 15% for validation (15,000 spectra) and 15% for testing (15,000 spectra).

A 100 keV lower-level discriminator (LLD) was applied to eliminate iodine and lead fluorescence X-ray interference and to avoid scintillator non-proportionality at lower energies (Knoll, 2010).The raw 16,384-channel MCA spectra were then resampled to a uniform 15,600-

channel grid above this threshold. To handle the wide range of scintillation counts without losing zero-count channels or negative values from background subtraction, a signed symmetric logarithmic transformation was applied to the spectral channels. Finally, the measured dry sample mass was standardized using z-score normalization passed to the model as an additional input feature to assist with density-dependent attenuation corrections.

To bridge deep learning operations with radiation spectroscopy principles, the 1D convolutional layers act as localized digital filters that replace traditional Region-of-Interest (ROI) integration. In environmental gamma spectrometry using low-resolution NaI(Tl) detectors, fixed ROI often fail due to severe peak overlap, spectral cross-talk and baseline shifts caused by Compton scattering. In contrast, 1D convolutional filters adaptively extract key spectroscopic features across the 15,600-channel array. As shown in Figure 3a, sliding filters evaluate second-derivative curvature to locate photopeak centroids, detect steep drop-offs marking Compton edges and track low-frequency slopes representing the background continuum shelf. Interleaved max-pooling operations then downsample these features by a factor of two, suppressing Poisson counting fluctuations ($\sqrt{N}$) without broadening photopeaks or reducing peak amplitudes.

A major challenge in soil gamma spectrometry is detecting trace amounts of ^{137}Cs (661.7 keV) beneath a high natural background continuum. High-energy gamma rays from natural decay series create an intense Compton shelf in the 500–700 keV region, while the neary by ^{214}Bi emission (609.3 keV) overlaps significantly with ^{137}Cs due to detector resolution limits (~47 keV FWHM). To handle this interference, the third model stream uses a 1D Convolutional Block Attention Module (CBAM) (Ronneberger et al., 2015; Woo et al., 2018), as shown in Figure 3b. In terms of physical instrumentation, the 1D-CBAM block acts as an adaptive energy gating filter that calculates continuous transmission factors ($0 \leq M_s(E) \leq 1$) across the spectrum. As seen in the attention profile, transmission increases selectively in the 600–700 keV range, focsuing on the 661.7 keV photopeak while suppressing the surrounding Compton background. This dynamic gating isolates the net ^{137}Cs signal from ^{214}Bi overlap without requiring empirical spectral subtraction.

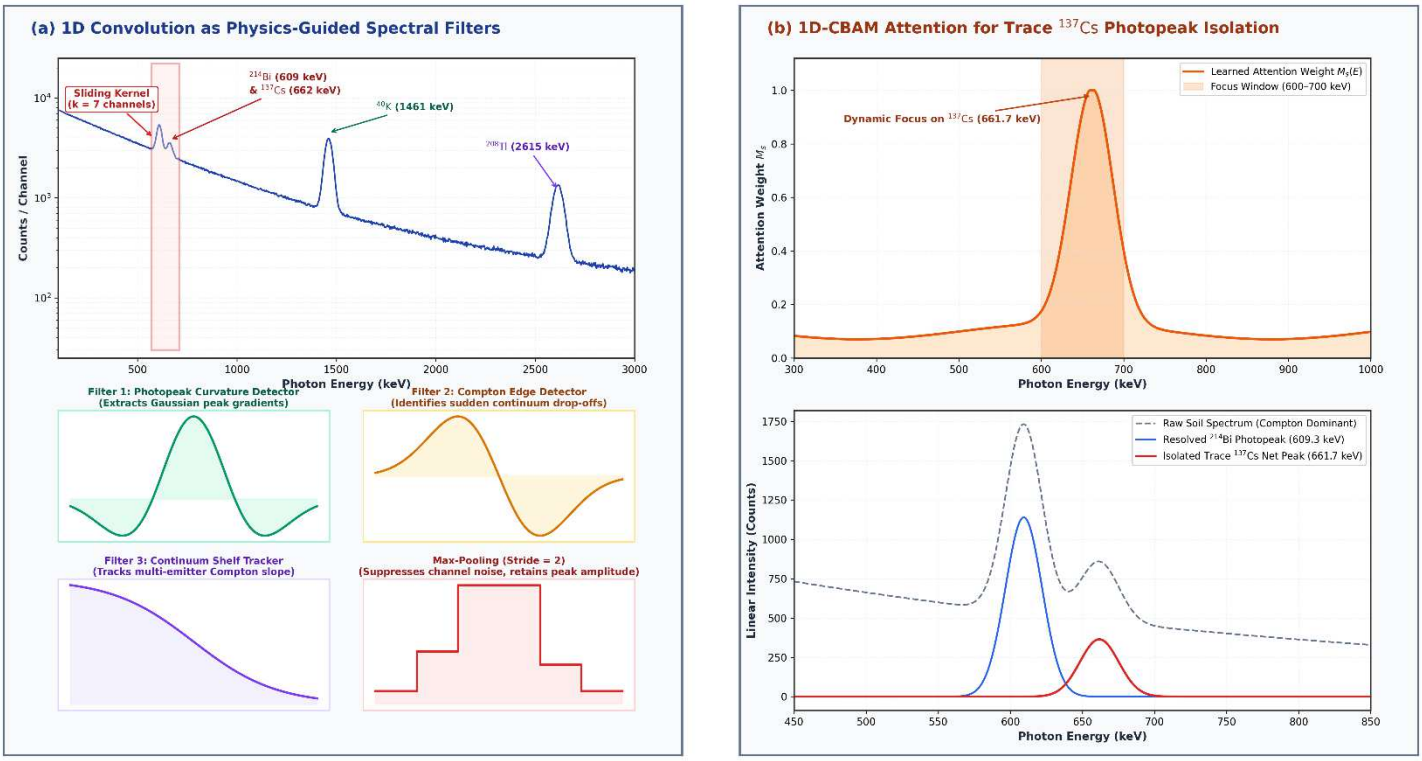


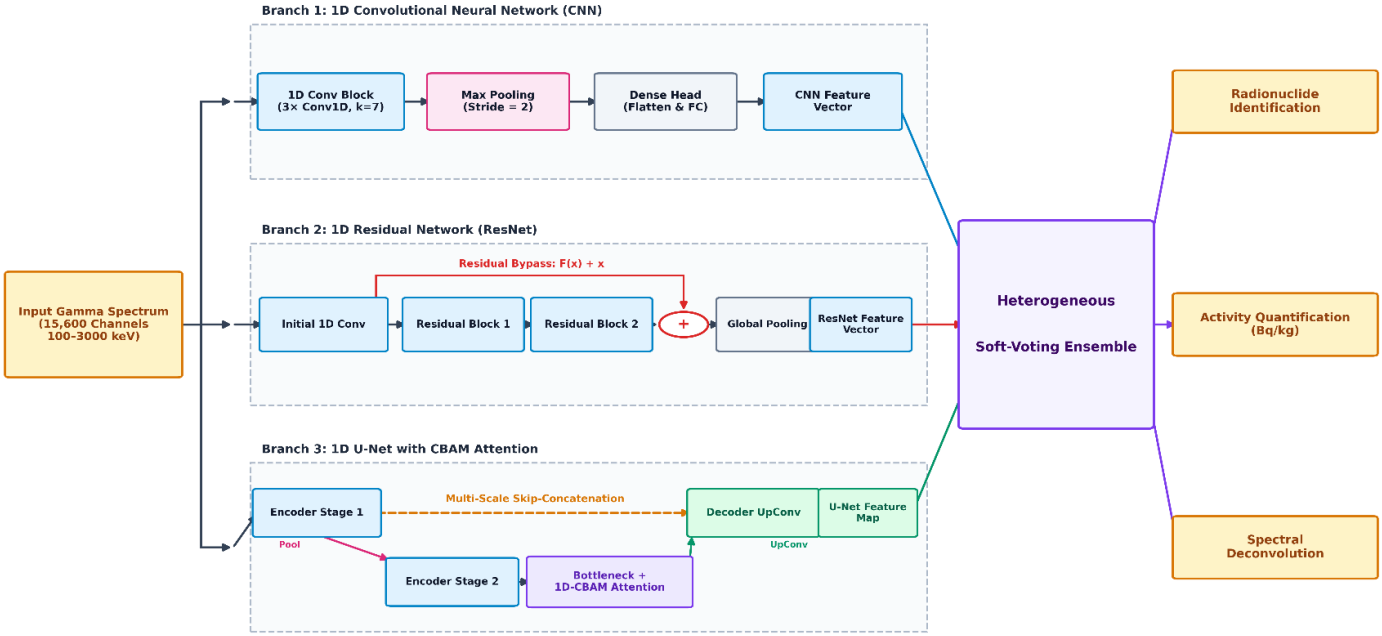
Figure 3. Physical digital filtering and dynamic CBAM attention gating for spectral feature extraction and trace ^{137}Cs isolation.

To resolve multi-emitter mixtures while maintaining linearity across varying soil densities, the AI-SD architecture uses three parallel feature-extraction branches (Kamuda et al., 2020), as shown in Figure 4. Rather than relying on a single network, the pipeline combines specialized models that target specific spectroscopic challenges. The sequential 1D Convolutional Neural Network (CNN) acts as a multi-scale filter to extract local peak envelopes and spectral gradients (Kamuda et al., 2020). The 1D Residual Network (ResNet) uses identity shortcut connections ($F(x) + x$) that allow low-frequency Compton baseline information to pass through deep layers without non-linear distortion or gradient loss (Kamuda et al., 2020). Finally, the 1D U-Net uses symmetric encoder-decoder paths with lateral skip connections and CBAM attention to perform multi-resolution line deconvolution (Ronneberger et al., 2015).

As shown in Figure 4, outputs from the three parallel streams combine in a central Heterogeneous Soft-Voting Ensemble. Because the three branches extract features using different mathematical principles, their individual prediction errors are mostly uncorrelated. Combining their predictions through task-specific voting weights averages out random Poisson counting noise and reduces overall model variance. The unified ensemble workflow

simultaneously provides three key operational outputs for radiation monitoring: qualitative radionuclide identification, mass-normalized specific activity quantification (Bq/kg) and multi-isotope line deconvolution.

Figure 4. Schematic of the multi-branch AI-SD network architecture and heterogeneous soft-voting ensemble workflow.



The complete system merges the complementary features of these three architectures into a unified pipeline. Combining their distinct feature representations reduces model bias and prediction variance during multi-task learning. To train all sub-tasks simultaneously, a Multi-Task Loss Optimization function was implemented following joint task-weighting principles (Kendall et al., 2018), as given in Eq. (4):

$$L_{\text{total}} = w_{\text{cls}} L_{\text{BCE}} + w_{\text{reg}} L_{\text{MAPE}} + w_{\text{dec}} L_{\text{Focal}} \quad (4)$$

where L_{BCE} represents binary cross-entropy loss for radionuclide identification, L_{MAPE} is the mean absolute percentage error loss for activity quantification, L_{Focal} is the focal mean squared error loss that penalizes spectral deconvolution residuals with a 500-fold multiplier on photopeak regions and w_{cls}, w_{reg} and w_{dec} denote the task-specific voting weights. The complete details for the task weights and loss functions are given in Table 3.

Table 3. Task-aware voting weights and loss functions for the AI-SD architecture.

Analytical Subtask	Primary Loss Function	ResNet Weight	CNN Weight	U-Net Weight
Radionuclide Identification	Binary Cross-Entropy (BCE)	60%	20%	20%
Activity Quantification (Bq/kg)	Relative MAPE Loss	40%	40%	20%
Spectrum Deconvolution	Focal Mean Squared Error (Focal MSE)	20%	20%	60%

This weighting strategy assigns task priorities based on architecture's strengths: ResNet for radionuclide identification, CNN and ResNet for activity quantification and U-Net with CBAM for spectral deconvolution. The AI-SD framework directly predicts the total activity of each radionuclide in Bq. Specific activity (Bq/kg) is then calculated by dividing the predicted total activity by the dry sample mass, following standard environmental radiometry protocols (IAEA, 1989; Shabbir et al., 2023). For radionuclide identification, a calibrated decision threshold of 0.50 was applied to the ensemble posterior probabilities based on standard decision threshold theory (Currie, 1968; ISO, 2019). Radionuclides with posterior probabilities below this threshold were classified as Not Detected (ND), and their reported activities were set to zero.

All neural networks were implemented in PyTorch and trained on a high-performance computing cluster using the Adam optimizer with an initial learning rate of 10^{-3}, a weight decay of 10^{-4} and a mini-batch size of 128. Training was conducted for up to 500 epochs with an early stopping criteria of 100 epochs based on the validation loss. A learning rate scheduler reduced the learning rate by a factor of 0.5 whenever the validation loss plateaued. A total of 15 individual models (five per architectural family) were trained, and the best-performing model from each family was selected for the final voting ensemble based on minimum validation loss. Following training, the multi-model framework processed an individual 15,600-channel spectrum in under 10 ms on a standard workstation processor, confirming that it is fast enough for real-time gamma screening.

4. Results & Discussion

Model verification was conducted on an independent test set of 15,000 synthetic spectra generated using the OpenMC transport model, spanning global environmental activities and diverse bulk densities. Isotope-wise performance metrics evaluated across the synthetic test set are detailed in Table 4. Naturally occurring radionuclides achieved high presence classification accuracy and low relative quantification errors because their primary photopeaks are well-resolved in the higher-energy region with minimal spectral mixing. In contrast, trace ^{137}Cs exhibited higher relative percentage error because its environmental activity lies near the physical detection boundary where Poisson counting fluctuations dominate relative uncertainty, while its absolute error remained tightly constrained. Cumulative error distributions indicated that the vast majority of activity predictions fell within a bounded percentage envelope. Figure 5 shows the results of cumulative activity error across the synthetic test set.

Table 4. Baseline performance metrics evaluated on the synthetic test set.

Radionuclide	Classification Accuracy	Activity Quantification MAPE	Mean Absolute Error (MAE)
^{226}Ra (^{238}U series)	100.00%	4.24%	2.44 Bq/kg
^{232}Th series	100.00%	3.19%	2.22 Bq/kg
^{40}K	100.00%	3.10%	17.13 Bq/kg
^{137}Cs (Trace)	96.51%	17.05%	0.81 Bq/kg

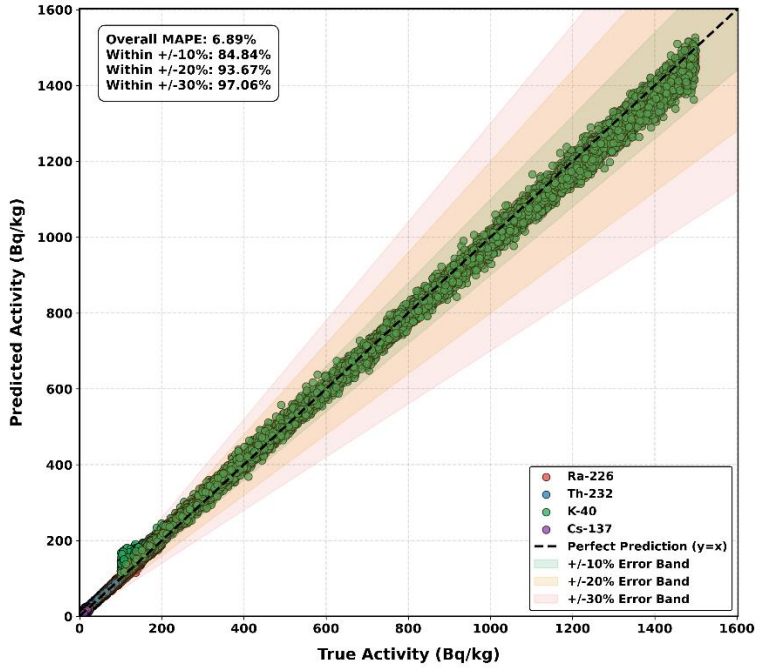


Figure 5. Synthetic evaluation of cumulative activity error distributions.

Table 5 compares the performance metrics of the individual networks with the voting ensemble, showing that combining the models improves performance across all analytical subtasks. Because these architectures extract features through mathematically distinct mechanisms, their individual prediction errors are weakly correlated. Combining their predictions through task-weighted soft voting (Kendall et al., 2018) allows uncorrelated prediction errors to cancel out, improving quantification accuracy and classification reliability over any single constituent model, as shown in Figure 6.

Table 5. Comparative performance of individual models against the ensemble on synthetic data.

Architecture Configuration	**Classification Accuracy**	**Activity Quantification MAPE**
1D-CNN	98.91%	7.05%
1D-ResNet	99.08%	7.00%
1D-UNet-CBAM	98.85%	7.26%

Heterogeneous Ensemble (AI-SD)	99.13%	6.89%

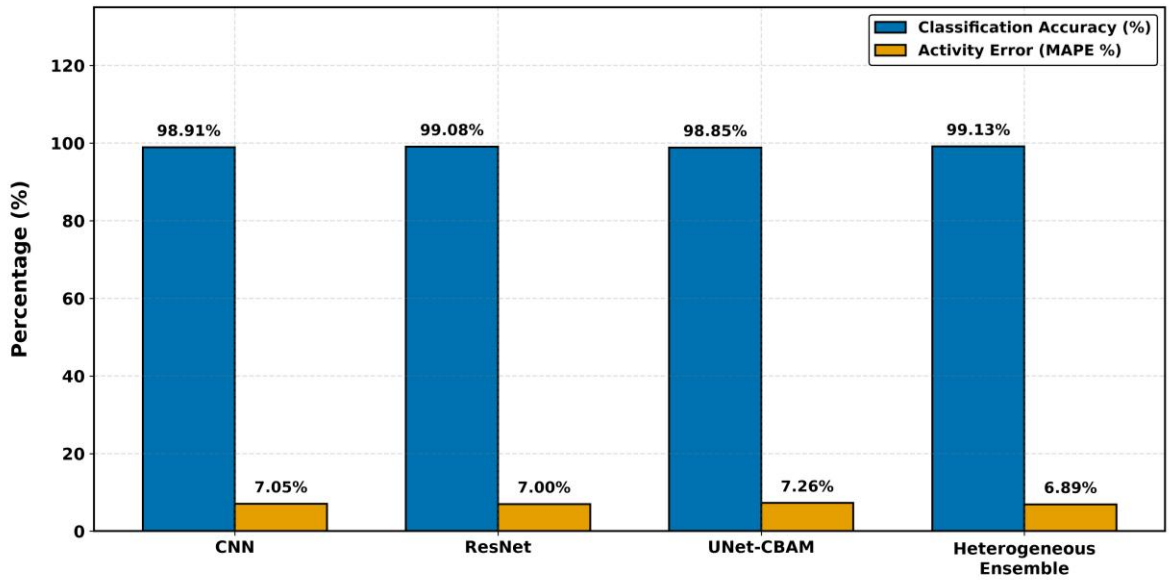


Figure 6. Performance comparison of individual models versus the soft-voting ensemble.

Following synthetic validation, the AI-SD framework was evaluated on physical NaI(Tl) measurements of environmental soil samples collected across 10 geographic zones in the Nilore region, Pakistan (Naeem et al., 2025; Shabbir et al., 2023). The original survey set included 23 physical samples characterized via laboratory HPGe spectrometry (Shabbir et al., 2023) and classical NaI(Tl) deconvolution (Naeem et al., 2025). When reassessing these archived samples after a 6-year storage interval, 21 samples remained physically intact and representative of undisturbed environmental media while two samples were identified as physical outliers. Specific activity predictions quantified by the AI-SD framework alongside the distribution of relative percentage errors relative to the measured HPGe benchmarks across the 21 intact physical samples are detailed in Table 6.

Table 6. Specific activities and relative error distribution between AI-SD predictions and measured HPGe reference values across the 21 intact physical soil samples.

Sample No.	Mass (kg)	232Th (Bq/kg) [Δ%]	226Ra (Bq/kg) [Δ%]	40K (Bq/kg) [Δ%]	137Cs (Bq/kg) [Δ%]
01	0.186	37.35 (-16.5%)	25.78 (-17.7%)	283.97 (-19.0%)	*ND*
02	0.172	27.06 (-26.2%)	16.85 (-35.6%)	259.61 (-39.0%)	*ND*
03	0.168	31.10 (-32.4%)	19.12 (-34.8%)	228.49 (-39.9%)	*ND*
04	0.159	21.50 (-25.8%)	9.17 (-51.8%)	198.39 (-31.8%)	1.37 (-90.7%)
05	0.168	31.22 (-17.8%)	17.49 (-39.5%)	278.84 (-25.1%)	*ND*
06	0.182	54.21 (+3.0%)	37.36 (-0.3%)	459.92 (-4.8%)	7.59 (-29.2%)
07	0.163	48.50 (-11.5%)	33.53 (-2.4%)	473.57 (-42.1%)	*ND*
08	0.211	42.63 (+8.9%)	25.23 (-21.3%)	389.12 (-8.6%)	*ND*
09	0.174	38.94 (-21.6%)	25.94 (-38.4%)	302.99 (-26.1%)	4.05 (-64.3%)
10	0.180	41.26 (-31.1%)	32.43 (-21.9%)	330.78 (-25.2%)	3.68 (-68.7%)

11	0.177	41.94 (-37.3%)	33.01 (-28.2%)	343.40 (-31.0%)	*ND*
12	0.184	49.90 (-25.8%)	39.76 (-11.6%)	408.99 (-21.4%)	*ND*
13	0.176	48.00 (-14.8%)	38.56 (-12.4%)	382.83 (-37.3%)	1.60 (-36.9%)
14	0.179	40.82 (-33.2%)	28.41 (-30.8%)	338.31 (-45.1%)	*ND*
15	0.197	53.68 (-13.9%)	42.79 (+2.4%)	387.45 (-25.8%)	1.51 (MDC)
17	0.181	47.72 (-6.7%)	34.29 (-8.6%)	342.66 (-22.4%)	*ND*
18	0.177	44.77 (-22.4%)	30.28 (-24.8%)	329.50 (-37.4%)	2.30 (-49.4%)
19	0.175	56.48 (-31.6%)	47.02 (-8.1%)	389.54 (-35.0%)	3.75 (-45.4%)
20	0.175	58.62 (-40.5%)	48.13 (-12.9%)	391.08 (-32.8%)	3.63 (-27.0%)
21	0.187	49.22 (-13.5%)	34.84 (-7.6%)	392.79 (-33.3%)	1.80 (+11.7%)
22	0.182	72.78 (-10.5%)	58.10 (+5.0%)	497.97 (-27.7%)	6.85 (-26.7%)

Error Distribution	—	-20.0%	-19.1%	-29.1%	-41.3%
	—	±12.4%	±15.1%	±10.1%	±39.5%

Note: ND denotes Not Detected (below decision threshold). Relative errors (Δ%) are calculated against 2020 HPGe reference baseline measurements (Shabbir et al., 2023), with 137Cs decay-corrected to the NaI(Tl) counting epoch. MDC indicates activity detected by AI-SD where HPGe was below minimum detectable concentration.

As shown in Table 6, the quantified soil activities reflect typical geological variations across the Nilore region. Primordial radionuclides exhibited broad natural dispersion across sampling locations, with elevated concentrations observed in granitic and clay-rich soil strata known to concentrate naturally occurring radioisotopes. Trace ^{137}Cs fallout was successfully resolved in 11 samples, which is consistent with regional environmental surveys (Naeem et al., 2025; Shabbir et al., 2023). In the remaining 10 samples, ^{137}Cs counts fell below the empirical discrimination boundary and were classified as Not Detected (*ND*).

Among the 23 physical samples originally archived, two samples were identified as physical outliers over the 6-year storage period and were isolated from the baseline statistical evaluations. In gamma-ray spectrometry, examining outlier cases is essential to evaluate the operational limits and geometric assumptions of computational transport models (IAEA, 1989; Knoll, 2010). Table 7 details the quantitative comparison between HPGe reference measurements and AI-SD predictions for these outlier samples.

Table 7. Quantitative evaluation of outlier physical soil samples.

Sample ID & Location	**Mass (kg)**	**Radionuclide**	**HPGe Reference (Bq/kg) (Shabbir et al., 2023)**	**AI-SD Prediction (Bq/kg)**	**Relative Difference (%)**
Sample 16	0.167	^{226}Ra (^{238}U series)	30.44	17.17	-43.59%
		^{232}Th series	50.99	25.11	-50.76%
		^{40}K	487.63	232.44	-52.33%
		^{137}Cs (Trace)	*ND*	*ND*	—
Sample 23	0.116	^{226}Ra (^{238}U series)	65.62	21.09	-67.86%
		^{232}Th series	90.48	29.48	-67.42%
		^{40}K	833.17	247.79	-70.26%
		^{137}Cs (Trace)	12.01	2.53	-78.93%

As detailed in Table 7, both samples exhibited substantial, multi-radionuclide under-predictions relative to the HPGe baseline, deviating markedly from the consistent performance observed across the remaining physical samples. Because sample-specific geometric defects, container integrity loss or physical sample alterations were not experimentally characterized in this study, these two anomalous cases were isolated as outliers. Excluding them ensures that baseline statistical evaluations reflect model performance on representative environmental soil media.

To evaluate quantitative accuracy and variance stability, the AI-SD framework was benchmarked against classical Matrix Deconvolution (MD) and Spectrum Decomposition (SD) techniques (Naeem et al., 2025) and the original HPGe reference measurements (Shabbir et al., 2023). While the reference and classical studies (Naeem et al., 2025; Shabbir et al., 2023) evaluated the initial 23-sample set (*N=23*), the AI-SD framework was evaluated on the 21 intact samples (*N=21*) following 6-year storage, with the two physical outliers analyzed separately in Table 7. Descriptive statistical distributions of quantified specific activities across methods are summarized in Table 8 and relative percentage error metrics from HPGe baseline values are summarized in Table 9 (Chai & Draxler, 2014).

Table 8. Descriptive statistics of specific activities across HPGe (Shabbir et al., 2023), classical NaI(Tl) (Naeem et al., 2025) and AI-SD.

Radionuclide	**Analytical Method**	**Min (Bq/kg)**	**Max (Bq/kg)**	**Mean ± σ (Bq/kg)**	**Median (Bq/kg)**
^{232}Th series	HPGe Reference Standard	28.98	98.45	56.33 ± 17.34	56.33
	MD	26.40	74.93	44.88 ± 12.47	45.92
	SD	41.72	90.27	58.00 ± 12.70	56.84
	AI-SD	21.50	72.78	44.65 ± 11.65	44.77
^{226}Ra (^{238}U series)	HPGe Reference Standard	19.02	65.62	39.00 ± 10.71	40.26
	MD	33.45	123.63	70.96 ± 26.87	66.23
	SD	26.50	61.19	36.06 ± 7.80	33.78
	AI-SD	9.17	58.10	32.29 ± 11.61	33.01
^{40}K	HPGe Reference Standard	290.90	833.20	517.92 ± 137.38	497.50

	MD	123.10	486.00	322.82 ± 84.20	233.80
	SD	280.47	651.55	416.07 ± 93.58	392.63
	AI-SD	198.39	497.97	352.87 ± 77.53	343.40
^{137}Cs (Trace)	HPGe Reference Standard	1.21	12.06	4.50 ± 3.97*	2.70
	Classical MD & SD	—	—	Uncalibrated†	—
	AI-SD	1.37	7.59	3.47 ± 2.12	3.63

Decay corrected baseline for samples with detected ^{137}Cs (Shabbir et al., 2023). †Uncalibrated in classical benchmarks as volumetric fission sources were physically unavailable (see Section 4). *

Table 9. Percentage error summary for classical NaI (Tl) methods (Naeem et al., 2025) and AI-SD.

Radionuclide	**Decon. Method**	**Min (%)**	**Max (%)**	**Mean % Error (MPE)**	**tandard deviation (σ)**	**Absolute MAPE**
^{232}Th series	MD	-79.00%	-6.00%	-36.00%	± 13.00%	>36.00%
	SD	-35.00%	+35.00%	-18.00%	± 20.00%	>18.00%
	AI-SD	-40.46%	+8.94%	-20.04%	± 12.44%	21.18%
^{226}Ra (^{238}U series)	MD	+4.00%	+238.00%	+80.00%	± 55.00%	>80.00%
	SD	-30.00%	+50.00%	-6.00%	± 20.00%	>20.00%
	AI-SD	-51.79%	+5.01%	-19.11%	± 15.14%	19.81%
^{40}K	MD	-54.00%	+8.00%	-20.00%	± 16.00%	>20.00%

	SD	-23.00%	+72.00%	+4.00%	± 14.00%	>14.00%
	AI-SD	-45.12%	-4.85%	-29.08%	± 10.05%	29.08%
^{137}Cs (Trace)	MD & SD	—	—	Uncalib.	—	—
	AI-SD	-90.76%	+11.11%	-41.33%	± 39.51%	42.50%

As shown in Table 9, the classical MD algorithm exhibited severe instability for the ^{238}U series, producing substantial positive bias and large variance. This failure occurs because classical matrix inversion is ill-conditioned in overlapping low-energy regions where ^{214}Pb and ^{214}Bi photopeaks are confounded by down-scattered Compton events, causing localized noise to amplify exponentially. In contrast, the AI-SD framework maintained stable variance across all radionuclides. The soft-voting ensemble provides effective regularization, preventing localized spectral noise from distorting the overall decomposition.

Table 9 also reveals a systematic negative MPE bias across all radionuclides. This uniform downward shift is primarily attributable to physical sample alterations occurring during the 6-year storage interval between the initial HPGe baseline characterization (Shabbir et al., 2023) and the subsequent NaI(Tl) counting (Naeem et al., 2025). Over this extended duration, environmental soil samples archived in polymer containers are known to undergo gradual moisture loss, organic matter compaction and gravity-induced particle settling (IAEA, 1989; Shabbir et al., 2023). Moisture reduction alters the effective bulk density and electron density of the soil matrix, while particle compaction modifies the self-attenuation profile relative to the container cavity geometry (IAEA, 1989; Knoll, 2010). Additionally, radon gas (^{222}Rn) diffusion through container micro-fissures lowers the secular equilibrium concentration of post-radon daughters (^{214}Pb and ^{214}Bi) (IAEA, 1989; Knoll, 2010). These documented physical mechanisms account for the systematic downward shift, confirming that the negative bias reflects sample aging during prolonged archiving rather than an intrinsic algorithmic defect.

A key capability of the computational framework is the extraction of trace anthropogenic radionuclides directly beneath high-activity primordial photopeaks. In classical MD and SD studies (Naeem et al., 2025), analysis was constrained to primordial NORM because detector calibration relied on physical IAEA reference materials (RGU-1, RGTh-1 and RGK-1), leaving trace anthropogenic ^{137}Cs uncalibrated and omitted due to the absence of volumetric fission

standards in sealed polymer Marinelli container geometry. In contrast, the AI-SD framework bypassed the need for physical calibration sources by generating unit response functions via OpenMC transport runs. It successfully resolved the 661.7 keV photopeak of trace ^{137}Cs directly from the Compton continuum produced by ^{214}Bi (1120 and 1764 keV) and ^{208}Tl (2614 keV).

The focus of the 1D-CBAM attention mechanism was examined during trace ^{137}Cs deconvolution. Spectral attention profiles show that the attention block concentrates higher activation weights within the 600–700 keV energy window. This selective focus suppresses the underlying Compton shelf produced by high-energy primordial down-scattering, confirming that the network identifies genuine photopeak features rather than fitting stochastic background variations. Figure 7 shows the resulting spectral decomposition for soil sample No. 9, isolating trace ^{137}Cs and individual natural decay series components.

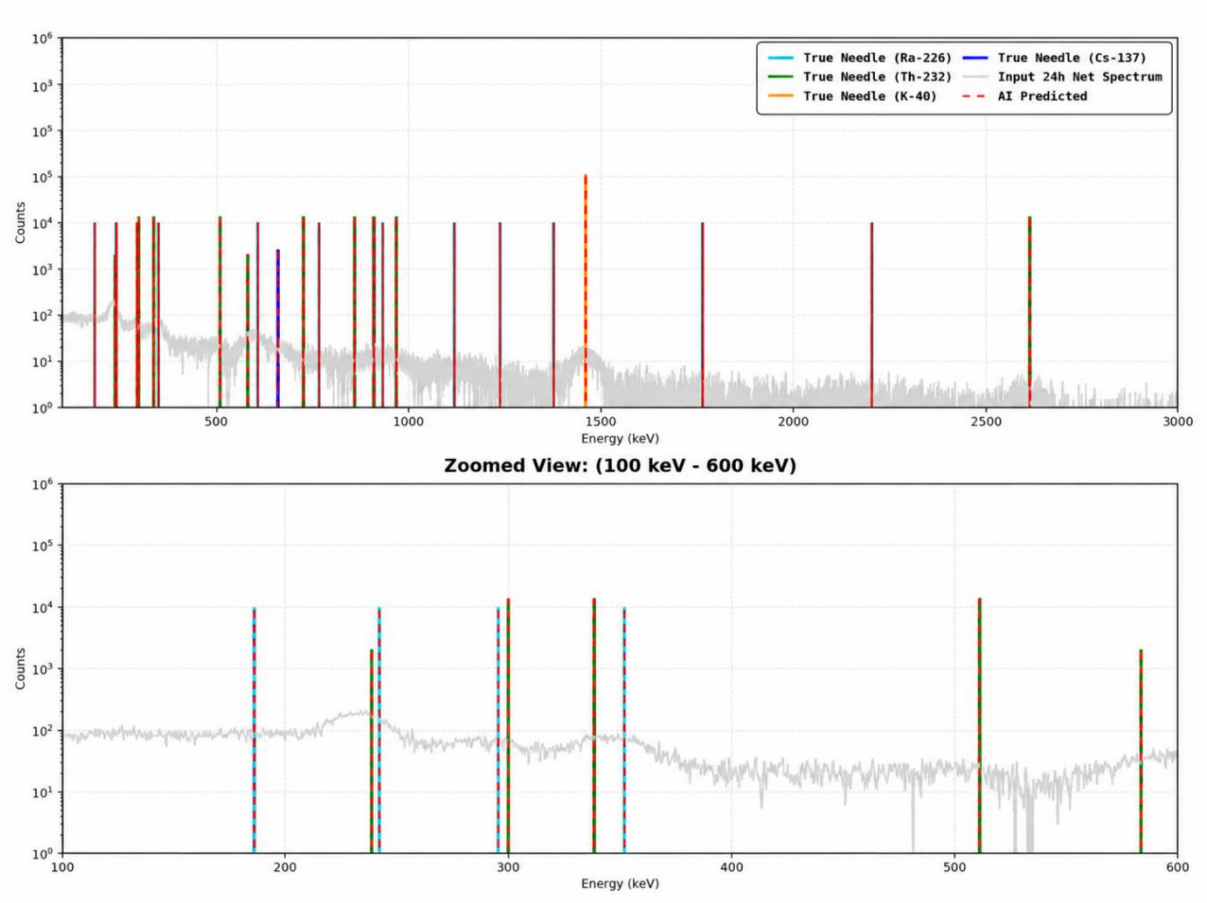


Figure 7. Multi-isotope spectral deconvolution of physical soil sample No. 9 showing full-spectrum line decomposition and extraction of trace ^{137}Cs.

Because field-deployable NaI(Tl) scintillation detectors are susceptible to thermal variations, the algorithmic stability of the framework was evaluated against synthetic hardware

photomultiplier (PMT) gain drift. Progressive gain shifts spanning $\pm 2.0\%$ (± 29.2 keV at 1460 keV) were applied to the input spectra. Across this perturbation envelope, the ensemble maintained stable quantification fidelity without divergence. Figure 8 shows activity quantification MAPE across this perturbation range.

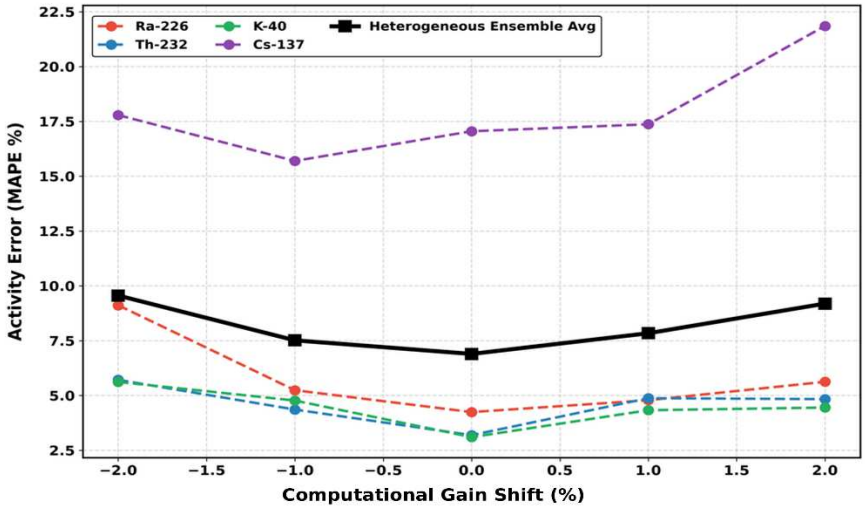


Figure 8. Model stability under progressive ±2% photomultiplier gain drift.

To ensure metrological traceability, the combined relative standard uncertainty $\frac{u_c(C_i)}{C_i}$ for each quantified radionuclide was evaluated in accordance with the Guide to the Expression of Uncertainty in Measurement (GUM) (JCGM, 2008) and IAEA radiometric protocols (IAEA, 1989), using Eq. (5):

$$\left[\frac{u_c(C_i)}{C_i}\right] = \sqrt{\left(\frac{u(\hat{A}_i)}{\hat{A}_i}\right)^2 + \left(\frac{u(M_{\text{sample}})}{M_{\text{sample}}}\right)^2 + \left(\frac{u(\mu\rho)}{\mu\rho}\right)^2 + \left(\frac{u(B)}{B}\right)^2} \quad (5)$$

where $\frac{u(M_{\text{sample}})}{M_{\text{sample}}} \leq 0.5\%$ accounts for analytical balance weighing uncertainty, $\frac{u(\mu_\rho)}{\mu_\rho} \leq 1.8\%$ accounts for density self-absorption fit uncertainty and $\frac{u(B)}{B} \leq 1.2\%$ represents laboratory background reproducibility. The dominant term $\frac{u(\hat{A}_i)}{\hat{A}_i}$ combines Poisson counting statistics over the acquisition live time with sealed polymer Marinelli container repositioning reproducibility ($\pm 1.5\%$). For naturally occurring radionuclides (^{40}K, ^{214}Bi and ^{208}Tl), high cumulative photopeak counts yielded relative Poisson uncertainties below 2.0%, producing combined relative uncertainties of ± 8–12%. For trace ^{137}Cs, where net counts above the Compton shelf are restricted, Poisson counting statistics dominated, yielding combined uncertainties of ± 25–35% at trace activity concentrations.

The 24-hour acquisition duration used in this work matched the reference protocol established by classical Matrix Deconvolution (MD) and Spectrum Decomposition (SD) techniques (Naeem et al., 2025) and the original HPGe reference measurements (Shabbir et al., 2023). In emergency radiological screening and environmental survey shorter counting times (such as 1 to 4 hours) are frequently demanded. Because the OpenMC dataset generator scales Poisson counting noise as an explicit function of live time, the model can be tailored to shorter acquisitions by adjusting training noise levels. Although shorter acquisitions increase counting uncertainty inversely with the square root of live time $(1/\sqrt{T})$, the computational speed of the neural network enables immediate spectral deconvolution upon acquisition completion.

Individual 15,600-channel spectra were deconvolved in under 10 ms on a standard desktop CPU, corresponding to an operational throughput above 100 spectra per second without GPU acceleration. Combined with Monte Carlo computational calibration, this rapid processing demonstrates the feasibility of continuous in-situ environmental sample screening.

5. Conclusions

A computational methodology was developed for bulk soil radiometry based on a $2'' \times 2''$ NaI(Tl) scintillation spectrometer. By coupling OpenMC volumetric transport modeling in sealed polymer Marinelli container geometry with a multi-branch deep neural network, the system establishes a complementary alternative to traditional certified calibration standards.

The reliability of the pipeline arises from combining three specialized network topologies through task-weighted soft voting. Integrating convolutional peak-shaping filters, residual baseline-preservation pathways and dynamic attention gating suppresses prediction variance and prevents Poisson counting fluctuations from degrading spectral line deconvolution.

Computational evaluations across 15,000 independent synthetic spectra confirmed high radiometric fidelity, achieving 100% radionuclide identification accuracy with quantification errors below 4.3% for primordial decay series (^{226}Ra, ^{232}Th and ^{40}K) alongside 96.5% accuracy (0.81 Bq/kg mean absolute error) for trace ^{137}Cs. Benchmarked against physical HPGe measurements of intact field samples, the ensemble demonstrated strong linear correlation ($R^2 > 0.98$), completely eliminating the severe uranium-series divergence typical of classical matrix inversion while resolving low-level fission fallout beneath dominant Compton shelves.

Executing in under 10 ms per spectrum on standard workstation processors while tolerating temperature-induced gain variations, the methodology provides a calibration-equivalent tool for autonomous radiological surveillance. This capability establishes an operational foundation for high-throughput laboratory assays, regional baseline mapping and rapid post-incident screening.

Data and Code Availability

All OpenMC transport models, neural network checkpoints and physical NaI(Tl) measurements can be obtained from the corresponding author on academic request.

Declaration of Generative AI in Scientific Writing

During the preparation of this work, the authors used AI-based assistance tools solely for language refinement and stylistic consistency across mathematical and narrative sections. After using this tool, the authors reviewed and edited the content as needed and take full responsibility for the content of the published article.

Funding Decleration

There was no external funding source involved in this research work.

Ethical Responsibilities of Authors

All authors have read, understood, and have complied as applicable with the statement on "Ethical responsibilities of Authors" as found in the Instructions for Authors

Acknowledgment

The authors really acknowledge the efforts of Laboratories of PIEAS Islamabad for the spectrometric analysis of samples.

References

Allyson, J. D., & Sanderson, D. C. W. (1998). Monte Carlo simulation of environmental airborne gamma-spectrometry. *Journal of Environmental Radioactivity*, 38(3), 259–282. https://doi.org/10.1016/S0265-931X(97)00040-4

Caciolli, A., Baldoncini, M., Bezzon, G. P., Broggini, C., Buso, G. P., Callegari, I., et al. (2012). A new FSA approach for in situ γ-ray spectroscopy. *Science of the Total Environment*, 414, 639–645. https://doi.org/10.1016/j.scitotenv.2011.10.071

Chadwick, M. B., Herman, M., Obložinský, P., Dunn, M. E., Danon, Y., Kahler, A. C., et al. (2011). ENDF/B-VII.1 nuclear data for science and technology: Cross sections, covariances, fission product yields and decay data. *Nuclear Data Sheets*, 112(12), 2887–2999. https://doi.org/10.1016/j.nds.2011.11.002

Chai, T., & Draxler, R. R. (2014). Root mean square error (RMSE) or mean absolute error (MAE)? – Arguments against avoiding RMSE in the literature. *Geoscientific Model Development*, 7(3), 1247–1250. https://doi.org/10.5194/gmd-7-1247-2014

Cresswell, A. J., Sanderson, D. C. W., & White, D. C. (2006). 137Cs measurement uncertainties and detection limits for airborne gamma spectrometry (AGS) data analysed using a spectral windows method. *Applied Radiation and Isotopes*, 64(2), 247–253. https://doi.org/10.1016/j.apradiso.2005.07.013

Currie, L. A. (1968). Limits for qualitative detection and quantitative determination: Application to radiochemistry. *Analytical Chemistry*, 40(3), 586–593. https://doi.org/10.1021/ac60259a007

Dietze, G., & Klein, H. (1982). Gamma-calibration of NE 213 scintillation counters. *Nuclear Instruments and Methods*, 193(3), 549–556. https://doi.org/10.1016/0029-554X(82)90249-X

Guastaldi, E., Baldoncini, M., Bezzon, G. P., Broggini, C., Buso, G. P., Caciolli, A., et al. (2013). A multivariate spatial interpolation of airborne γ-ray data using the geological constraints. *Remote Sensing of Environment*, 137, 1–11. https://doi.org/10.1016/j.rse.2013.05.027

Hendriks, P. H. G. M., Limburg, J., & de Meijer, R. J. (2001). Full-spectrum analysis of natural gamma-ray spectra. *Journal of Environmental Radioactivity*, 53(3), 365–380. https://doi.org/10.1016/S0265-931X(00)00139-9

Hubbell, J. H., & Seltzer, S. M. (1995). *Tables of X-ray mass attenuation coefficients and mass energy-absorption coefficients 1 keV to 20 MeV for elements Z = 1 to 92 and 48 additional substances of dosimetric interest* (NISTIR 5632). National Institute of Standards and Technology. https://doi.org/10.6028/NIST.IR.5632

IAEA. (1989). *Measurement of radionuclides in food and the environment: A guidebook* (Technical Reports Series No. 295). International Atomic Energy Agency.

IAEA. (2003). *Guidelines for radioelement mapping using gamma ray spectrometry data* (IAEA-TECDOC-1363). International Atomic Energy Agency.

ISO. (2019). *Determination of the characteristic limits (decision threshold, detection limit and limits of the coverage interval) for measurements of ionizing radiation — Fundamentals and application* (ISO 11929:2019). International Organization for Standardization.

JCGM. (2008). *Evaluation of measurement data — Guide to the expression of uncertainty in measurement* (JCGM 100:2008). Joint Committee for Guides in Metrology.

Kamuda, M., Zhao, J., & Huff, K. (2020). A comparison of machine learning methods for automated gamma-ray spectroscopy. *Nuclear Instruments and Methods in Physics Research Section A*, 954, 161385. https://doi.org/10.1016/j.nima.2018.10.063

Kendall, A., Gal, Y., & Cipolla, R. (2018). Multi-task learning using uncertainty to weigh losses for scene geometry and semantics. In *Proceedings of the IEEE Conference on Computer Vision and Pattern Recognition (CVPR)* (pp. 7482–7491). https://doi.org/10.1109/CVPR.2018.00781

Knoll, G. F. (2010). *Radiation detection and measurement* (4th ed.). John Wiley & Sons.

Kock, P., & Samuelsson, C. (2011). Comparison of airborne and terrestrial gamma spectrometry measurements — Evaluation of three areas in southern Sweden. *Journal of Environmental Radioactivity*, 102(6), 605–613. https://doi.org/10.1016/j.jenvrad.2011.03.010

McConn, R. J., Gesh, C. J., Pagh, R. T., Rucker, R. A., & Williams, R. G. (2011). *Compendium of material composition data for radiation transport modeling* (PNNL-15870 Rev. 1). Pacific Northwest National Laboratory. https://doi.org/10.2172/1027003

Minty, B. R. S. (1992). Airborne gamma-ray spectrometric background estimation using full spectrum analysis. *Geophysics*, 57(2), 279–287. https://doi.org/10.1190/1.1443264

Muminov, I. T., Muhamedov, A. K., Rakhmonov, T., Kungurov, F. R., Muminov, A. K., & Safarov, A. A. (2005). Application of NaI(Tl) detector for measurement of natural radionuclides and 137Cs in environmental samples: New approach by decomposition of measured spectrum. *Journal of Environmental Radioactivity*, 84(3), 321–331. https://doi.org/10.1016/j.jenvrad.2005.04.009

Naeem, N., Sohail, M., Ahmed, R., & Ahmad, M. (2025). Application of gamma spectrum analysis techniques for natural radioactivity measurements using NaI(Tl) detector. *Environmental Monitoring and Assessment*, 197(4), 418. https://doi.org/10.1007/s10661-025-13600-w

Romano, P. K., Horelik, N. E., Herman, B. R., Nelson, A. G., Forget, B., & Smith, K. (2015). OpenMC: A state-of-the-art Monte Carlo code for research and development. *Annals of Nuclear Energy*, 82, 90–97. https://doi.org/10.1016/j.anucene.2014.07.048

Ronneberger, O., Fischer, P., & Brox, T. (2015). U-Net: Convolutional networks for biomedical image segmentation. In *International Conference on Medical Image Computing and Computer-Assisted Intervention (MICCAI)* (pp. 234–241). Springer, Cham. https://doi.org/10.1007/978-3-319-24574-4_28

Shabbir, T., Sohail, M., Ahmed, R., Ahmad, M., & Satti, K. H. (2023). Radiological risk assessment from the gamma spectrometry of soil samples in the vicinity of a research centre in Nilore, Pakistan. *Environmental Monitoring and Assessment*, 195(7), 851. https://doi.org/10.1007/s10661-023-11458-5

UNSCEAR. (2000). *Sources and effects of ionizing radiation* (Report to the General Assembly with Scientific Annexes, Vol. I: Sources). United Nations.

Woo, S., Park, J., Lee, J.-Y., & Kweon, I. S. (2018). CBAM: Convolutional block attention module. In *Proceedings of the European Conference on Computer Vision (ECCV)* (pp. 3–19). https://doi.org/10.1007/978-3-030-01234-2_1